High-precision astrometry laboratory demonstration for exoplanet detection using a diffractive pupil telescope

Eduardo A. Bendek[a], S. Mark Ammons[b], Ruslan Belikov[c], Eugene Pluzhnik[c], Olivier Guyon[a]
[a]University of Arizona, Steward Observatory, 933 N Cherry Ave, Tucson, AZ, USA 85721;
[b]Lawrence Livermore National Laboratory, 7000 East Ave, Livermore, CA 94550;
[b]NASA Ames Research Center, Moffett Field, CA 94035, USA

ABSTRACT

Detection of earth-size exoplanets using the astrometric signal of the host star requires sub microarcsecond measurement precision. One major challenge in achieving this precision using a medium-size (<2-m) space telescope is the calibration of dynamic distortions. The researchers propose a diffractive pupil technique that uses an array of approximately 5um dots on the primary mirror that generate polychromatic diffraction spikes in the focal plane. The diffraction spikes encode optical distortions in the optical system and may be used to calibrate astrometric measurements. This concept can be used simultaneously with coronagraphy for exhaustive characterization of exoplanets (mass, spectra, orbit). At the University of Arizona, a high precision astrometry laboratory was developed to demonstrate the capabilities of this diffractive pupil concept. The researchers aim to demonstrate that the diffractive pupil can improve current limiting factors of astrometric accuracy. This paper describes this laboratory and the results showing that this technique can effectively calibrate dynamic distortions.

Keywords: Distortion, diffractive pupil, high-precision astrometry, exoplanet detection.

1. INTRODUCTION

Philosophers and scientists have discussed the question about life beyond the earth for many years. However, it was not until 1988, when the first exoplanet was detected[1] using an indirect observation technique called radial velocity, that the possibility of other habitable planets around the universe became a real possibility. The second exoplanet was discovered in 1992, and since then the detection of exoplanets has become a major research subject in astronomy. In the last ten years more sensitive instrumentation has been developed for both ground and space telescopes with technologies that allow detection and characterization of Earth-like planets, with a longer-term goal of assessing habitability and finding life outside the solar system.

Exoplanet characterization will inevitably rely on high quality spectroscopy, which fundamentally requires direct imaging in order to separate the planet's light from bright starlight. Direct imaging and spectroscopy will provide information about the atmosphere composition and dynamics (weather), as well as planet rotation period and an estimate of its diameter. Mass determination is also critical, as it defines the planet's ability to retain an atmosphere, its surface gravity, and the planet internal composition (water world, rocky, Neptune-like, or mostly gaseous).

More recently, the direct detection of planetary system such as Beta Pictoris, HR8799 and the (indirect) detection of a large number of new exoplanet candidates by the Kepler mission have motivated not only scientists but also the general public to wonder about other habitable worlds and consider them as a real possibility. On the other hand, high precision astrometry of a host star would allow obtaining the exoplanet mass and orbit.

While direct imaging and astrometry are suitable to identify nearby planets, both are required for unambiguous characterization of potentially habitable worlds[2]. It has been so far assumed that coronagraphic imaging/spectroscopic measurement and mass determination require two separate missions. The researchers recently proposed an approach that combines the two critical techniques using a single space telescope in which light is simultaneously fed to a narrow field coronagraph for exoplanet imaging and spectroscopy and a wide field astrometric camera for imaging a wide annulus

around the central field for mass measurement with astrometry. The astrometric measurement is calibrated using a concept proposed by Guyon et al.[3] which uses a diffracting part of the bright starlight into narrow diffraction spikes, generated by a periodic grid of dots, which are deposited on the telescope's primary mirror. The technique allows high precision astrometric measurement of the central star position using the large number of faint background stars as a reference. It is immune from image distortions in optics or detectors, as these distortions equally affect the diffraction spikes and the background stars, and the proposed astrometric measurement is a differential signal between the position of the diffraction spikes and the background stars.

In this paper, we present the first laboratory results of this technique. In section 2 we present a summary of the concept, and in section 3 we describe the design drivers of the main components of the laboratory. In section 4, we present the data reduction algorithm used to retrieve the distortion calibration map from the images. Finally, in section 5 we show the laboratory astrometric results together with the results of compatibility with high contrast imaging.

2. THE DIFFRACTIVE PUPIL CONCEPT

A concept to achieve sub-μas accuracy astrometry using a diffractive pupil that calibrates dynamic distortion was proposed[3]. In this concept a periodic array of small dots is imprinted in the primary mirror, which is also the pupil, of the telescope. These dots create diffraction and generate a new array of dot with inverse spatial frequency as predicted by the Fraunhofer far field relationship

$$U_0(x_0,y_0) = -\frac{je^{jkz_0}}{\lambda z_0}\exp\left[j\frac{k}{2z_0}(x_0^2+y_0^2)\right]F_{\eta=\frac{y_0}{\lambda z_0}}F_{\xi=\frac{x_0}{\lambda z_0}}\left[U_S^+(x_s,y_s)\right] \quad (1)$$

When the system is illuminated by polychromatic light, such as a real star, each spot on the image plane gets replicated for each wavelength at a different radial distance given the $1/\lambda$ dependence of the transform variables ξ and η. As a result, diffraction spikes are created on the image plane. The electric field at the pupil U_S^+ can be modeled as a plane wave incident on a circular aperture, and the dots correspond to a small circular obstruction convolved with an array of delta functions.

The spikes are the result of the convolution the array of deltas in Fourier space and the image plane PSF of the pupil given by the diameter of the primary mirror. Finally, the dot size modulates the intensity of the spikes. As a result, the spikes location and periodicity is defined by the geometry and spacing of the dots on the pupil. The stability of the spikes depends on the mechanical stability of the dots on the pupil. Therefore, it is critical to generate the dots directly on the mirror coating.

The spikes distort according to changes in the optics and therefore they can be used to map the dynamic distortions of the optical system, and therefore they mitigate this term from the astrometric error budget. The astrometric signal of the central star is now measured by comparing the position of the diffraction spikes to the background stars instead of directly to the host star PSF.

The distortion calibration concept is described in Figure 1. An ideal imaging system is shown in the top row, and the distance of each star is measured to closest spike. A real system with distortions is shown in the lower row. In this case distortions affect the spikes as well as removing this error by measuring the distance from the background star to the closest spike and not to a pixel. The top row shows how the astrometric signal of the host star will appear as a relative spike with respect to the background star field. In the presence of dynamic distortions between measurements, as shown in the second row of Figure 1, the pixel location of a star is biased by the distortions; however, if the distance is measured to the spike, this effect is calibrated.

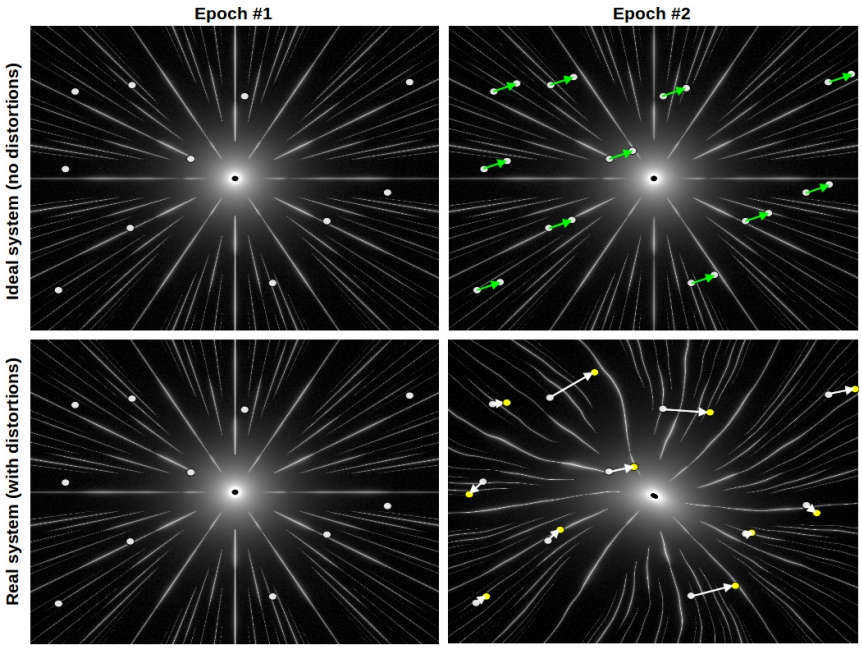

Figure 1. This figure shows the astrometry calibration algorithm using the diffractive spikes. On the top row two measurements or epochs are shown for a perfect system. An astrometric signal creates a uniform differential motion of the pixels and the reference stars. In the lower row a system that is affected by distortions cause errors in the astrometric measurement, which can be calibrated using the diffractive spikes as a reference.

3. THE HIGH PRECISION ASTROMETRY LABORATORY

3.1 Design Goals

The main goal of this laboratory is to demonstrate the ability of the diffractive pupil to calibrate field distortions, hence improving the astrometric accuracy of the telescope where the pupil is installed. In a photon-limited regime, the precision of the astrometric measurement is proportional to the width of the diffraction-limit of the telescope. For a scaled-down testbed intending to approximate the performance of a space telescope, assuming that the wavelengths used are comparable, the ultimate testbed precision is simply the ratio of the primary mirror diameters multiplied by the required single-axis single-epoch precision of the space-based mission. If a 0.2 μas performance on a 1.4 m space telescope[3] is compared with a 16mm diameter testbed primary mirror, an ultimate measurement precision of (1,400mm/16 mm) 0.2μas ~18μas can be achieved using state of the art centroiding techniques and telescope roll to average pixel errors. At this stage none of the techniques have been implemented on the laboratory; therefore, we expect results significantly larger in the order of 500μas. However, 18μas set the ultimate limit for the astrometric accuracy.

Another goal of this laboratory is to prove that the diffractive pupil enables high precision astrometry of a bright star, even if the star is not visible or saturated, enabling the telescope to perform astrometry with a wide field camera and direct imaging simultaneously by sending the light in the Inner Working Angle (IWA) region to a coronagraph. This is possible only using the diffractive spikes, which contain all the astrometric information of the host star.

This work also aims to demonstrate the manufacturability of the diffractive mirrors and find if there is any light contamination of the IWA region that would be used for direct imaging by light diffracted at the pupil. This kind of effect can be caused by low frequency changes in the dots location due to manufacturability issues.

In order to accomplish the test successfully, the astrometric stability of the reference grid of stars is of the utmost importance. For this testbed, the instrumental jitter is determined by non-systematic motion of reference stars at the μas (nanometer) level after larger systematic thermal expansions are compensated, either by calibration or thermal stabilization of the bench. Small-scale motions may be introduced when temperature changes through small-scale variations in the Coefficient of Thermal Expansion (CTE) in the star field substrate. Small-scale CTE variations will

introduce uncorrelated errors that average down with the number of stars. CTE variation over larger scales will cause astrometric motion that is correlated from star to star and will not necessarily average down.

For the final configuration of the testbed, the usage of zerodur will be used as the star field substrate. Also, the temperature in the enclosure will be controlled within 100mK. For a mean CTE of 2e-8 for zerodur and temperature stability of 100mK, the overall RMS expansion will be ~ 15pm at the edge of the field, corresponding to an amplitude of approximately 5μas or $1.6x10^{-6}$ pixels, which is smaller than the desired precision of 18μas. The residual following subtraction of overall expansion or contraction will be much less than 1μas. Unfortunately, the contribution due to small scale CTE variation in Zerodur is not well constrained at this time, but since it averages down with the number of stars, there is reason to believe it will be less than the amplitude of the overall expansion and contraction.

3.2 The Optical System

The optical system was designed considering the same top-level requirements of a space-based mission devoted to exoplanet detection using astrometric measurements of the host star, as described in previous publications[4]. The top-level requirements for a telescope using this technique are the following: First, a uniform grid of holes on the coating of the primary mirror. These holes will generate diffraction that will be imaged as spikes in the focal plane under polychromatic illumination. Second, the aperture stop of the telescope must be located at the primary mirror. Finally, only reflective optical elements can be used to avoid spectrum changes on the spikes caused by transmissive optical elements. Additionally, the optical system should be able to produce diffraction-limited images for a field of at least 0.5 deg^2 to provide enough background stars using an off-axis optical configuration to avoid diffraction from the central obscuration and the secondary holder spider. Also it is necessary to simulate telescope roll in order to mitigate detector effects such as noise and responsivity, and, despite that this requirement does not affect the real telescope optics, it imposes a challenging requirement for the design of the optical system in the laboratory.

The top-level requirements and the real system value achieved for the laboratory have been defined and are listed in Table 1. The CCD camera, an Apogee ALTA U16000 with a pixel size of 7.4μm, and two 8" diameter f/5 parabolic mirrors were set as fixed parameters for the design of the optical system. These two basic constraints, and the Nyquist sampling specification, require a Point Spread Function (PSF) larger than 2 pixels or 14.8μm, resulting in a system with f/# larger than 24. The star simulator uses pinholes to simulate the background stars and their sizes. The pinholes are set to 5μm due to manufacturability constraints, defining a minimum distance from the source to the pupil of the optical system.

Table 1. Top-level requirements of the optical system for the astrometry test bed

Astrometry test bed optical system top-level requirements and real system values.

Requirement	Requirement	Achieved value
Wavefront error (RMS)	< λ/4 (Diffraction limited)	λ/7 for 1.4˚ FFoV at 550nm
Operational wavelength	350 to 900 nm	350 to 900 nm
Sampling	> Nyquist	24μm FWHM PSF (3.1 pixels)
Optics type	Reflective only	Yes
Pupil type	Dotted diffractive pupil	Hexagonal 5x50 μm dot pattern
Pupil Illumination uniformity	90%	90%
FOV	As large as possible	1.4˚
No central obscuration	Off-axis design chosen	Yes
Telescope roll simulation	Rotation > 360 degree	Yes

Several optical layouts were attempted to meet the top-level requirements of the astrometry test bed and maximize the unvignetted FOV and pupil size. After testing and building different configurations that proved challenging to align, a design using two off-axis parabolas (OAP) was chosen. The system was designed to image a source located 550mm away from the first optical surface, which is a flat folding mirror and also the pupil and stop of the system. This mirror simulates the primary mirror of the telescope and features the dot pattern that generates the diffraction spikes. The mirror sends the light to the first off-axis parabola, which is located at a distance from the source that matches the focal length of the parabola to collimate the light of the source after reflection. This matching helps to adjust the distance of the

second off-axis parabola, minimizing the impact on the wavefront error. The second off-axis parabola sends a converging beam to the camera using a folding flat mirror to optimize the space on the breadboard and maximize FOV.

A model of the system was created in ZEMAX to design and optimize the selected configuration using guidelines suggested in the literature.[5] The mirrors are off-axis parabolas by design; however, the real system and the ZEMAX model were implemented with full parabolas because of cost and alignment simplicity reasons. The optimization routine was used in sequential steps, releasing variables as the system was converging to the optimum, achieving diffraction limited performance over a FOV > 12 x 12mm or 1.4 degrees with a pupil size of 16 mm.

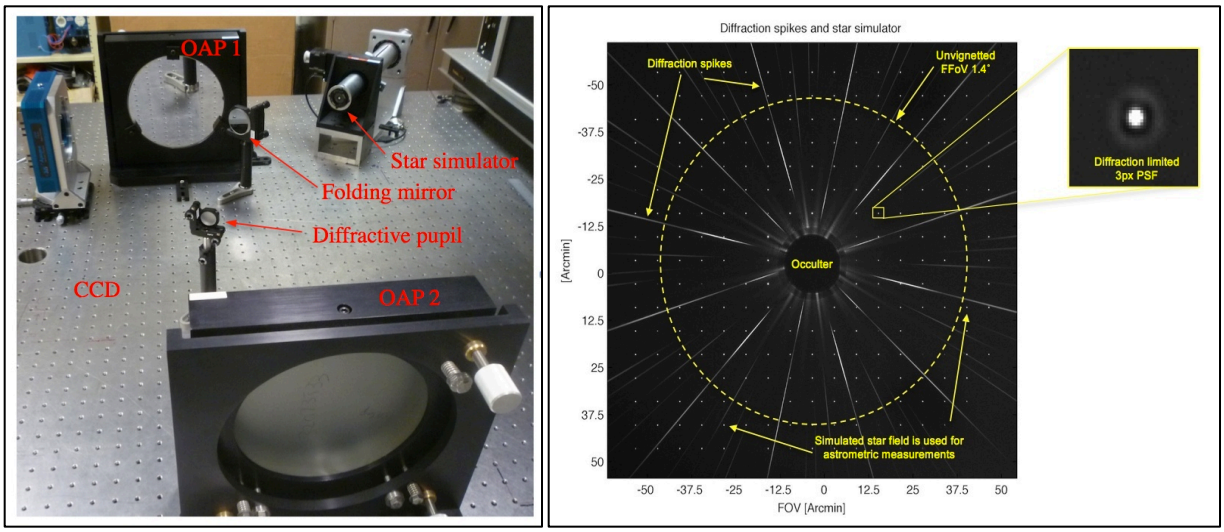

Figure 2. On the left a picture of the laboratory optics is shown. On the right a real image showing the spikes and the background stars is presented.

The diffraction limit of the system is 24µm at 550nm wavelength. The performance on-axis of the system is excellent, as expected for an off-axis parabolic design; however, the FOV of the system is limited by vignetting of the beam and by increasing astigmatism contribution to the wavefront error as the off-axis angle increases. The optical interface with the star simulator defines the entrance pupil location and stop at 550mm from the object, with a diameter of 16mm and an optical axis height of 158.75 mm.

3.3 Dotted Pupil Mask Design and Fabrication

The first mask master set was fabricated by the Colorado Nanofabrication Lab (CNL) using a chrome-on-glass composition that is exposed with a direct laser-writing tool. A thin layer of resist is coated on the chrome and the laser exposes the pattern of holes in the positive resist, which is washed away in the developing solution. The substrate is then placed in an etch solution; therefore, where the resist is washed away the chrome is etched. The result after this process is a pattern of etched holes in an otherwise solid chrome film. The master pattern is then used in a modified mask aligner, where the master mask is brought in contact with a resist-coated aluminum mirror. The pattern is transferred onto the mirror's resist by exposing the combination with a UV lamp. Then, the developing and etching process is repeated to obtain holes in the aluminum mirror surface. The first pupil mask shown in Figure 3 was manufactured using this process. However, this process cannot be implemented on a curved aspheric mirror since the master will not make proper contact with the mirror resist.

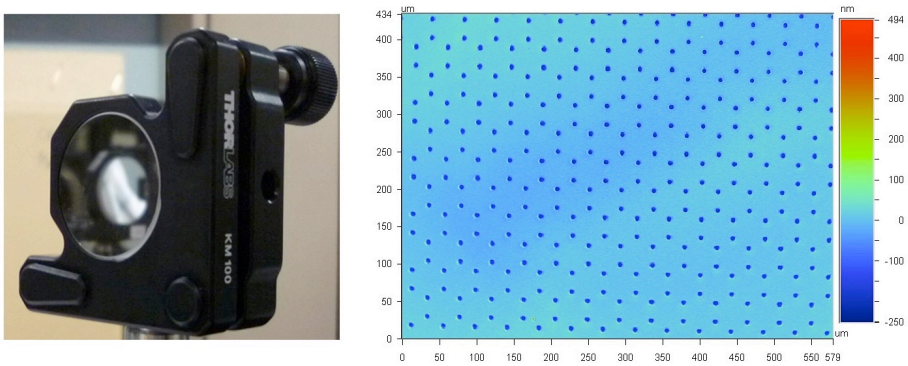

Figure 3. The image on the left shows a picture of the pupil dotted mirror mounted in the optical system, the image on the right shows a VEECO microscope image of the pupil mirror coating where the hexagonal dotted pattern be clearly seen. The dots are 5µm in diameter and hexagons are 50µm wide each.

3.4 Star Field Simulator and Astrometric Signal

An illumination source that simulates a star field containing a brighter central star has been designed and built to simulate the operational conditions of the real mission. This brighter star is the candidate to host an exoplanet, hence the star simulator should be able to generate the respective astrometric signal on this source. The design of the star field simulator is driven by the following requirements: First, it is necessary to simulate a stable star field since it will limit how precisely the performance of this technique can be assessed. The ultimate desired stability of the field is in the order of 5µas after removing systematic errors on the simulator. Second, considering that the brightness ratio of the spikes versus the central star is in the order of 10^{-8}, the central star must be 10^4 brighter than the field stars to be able generate spikes with a SNR of 2 without saturating the background field stars, which occurs at $6.5x10^4$ counts. Third, the pupil must be uniformly illuminated by all the sources in the star simulator located 550 mm away from the pupil. A uniformity requirement of 90% was defined. Fourth, the star simulator has to rotate for at least 360 degrees to simulate telescope roll, which is intended to average detector effects. Finally, the star simulator has to provide a means to generate small astrometric signals by moving the central star PSF.

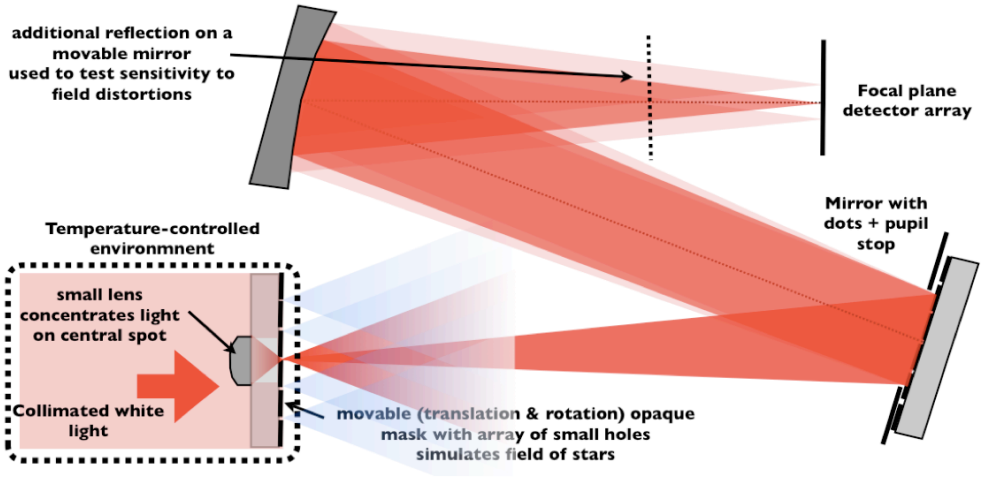

Figure 4. Conceptual drawing of the star simulator and the imaging system. Collimated white light illuminates the backside of a fused silica flat window. The front side is coated with chrome where an array of 17x17 holes, 5µm in diameter each are imprinted by lithography. On the back of the substrate there is a small concentrator lens that is precisely glued to focus the light on the central pinhole making this star much brighter, but with the same diffraction pattern.

Illuminating the backside of a fused silica flat window with collimated white light creates the star field. The front side is coated with chrome, where an array of 17 by 17 holes 5µm in diameter are imprinted by lithography. On the back of the substrate there is a small concentrator lens that is precisely glued to focus the light on the central pinhole, or star, enhancing its brightness by a factor $1.5x10^4$ without affecting the diffraction angle that illuminates the pupil. This concept is illustrated in Figure 4.

The collimated beam needed to illuminate the star field mask is obtained by connecting a light source to a fiber fed in one end of a 500mm tube. Then, the light from the fiber reaches a couple of achromatic doublets, where the second of them can slide to adjust collimation. A ZEMAX model of this system is shown in Figure 5. This concept also allows the creation of an astrometric signal by translating the fiber source on a plane perpendicular to the optical axis on the back of tube. When the fiber became off-axis with respect to the achromatic doublets, a slight tilt is introduced on the wave-front causing a motion of the central star PSF after going through the concentrator lens, as is shown in the lower left images of Figure 5. The system was designed to reduce the motion of the central star PSF by a factor of 50 with respect to the fiber motion, increasing the accuracy and stability of the simulated star. Finally, the illumination system and the star field mask are required to rotate to simulate the telescope roll used to average out pixel errors. As a result it was necessary to mount the star simulator in a rotation stage.

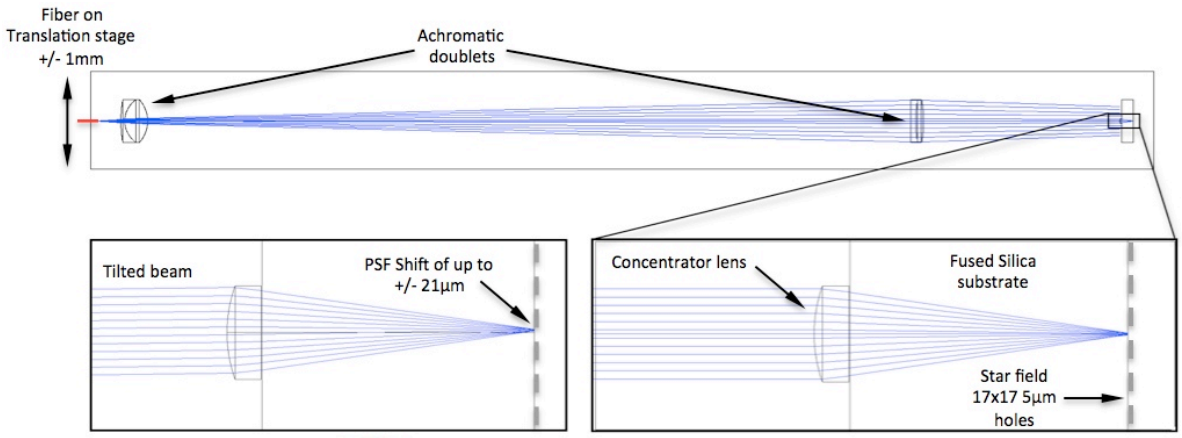

Figure 5. ZEMAX model of the light source, the star simulator substrate and the concentrator lens that increases the brightness of the central star by a factor of $1.5x10^4$ but conserves the diffraction angle by having the same hole size in the coating. The lower image on the left shows how the astrometric signal is generated. In this case, a 1mm displacement of the fiber source translates into 24µm motion of the central star PSF.

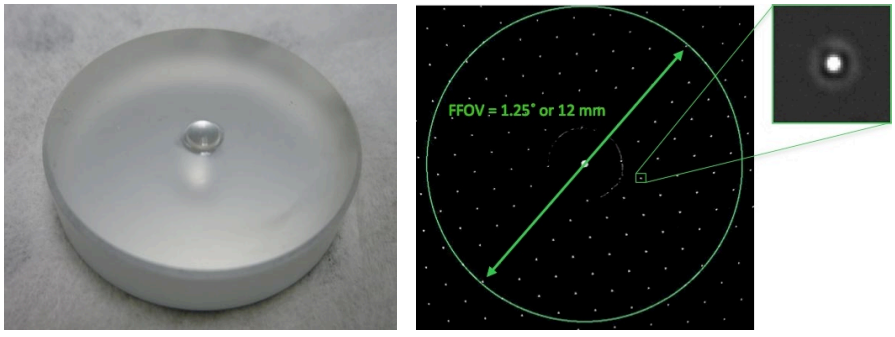

Figure 6. The image on the left shows the substrate with the concentrator lens glued in the back. The image on the right shows the simulated star field.

4. DATA REDUCTION

4.1 Data Reduction Algorithm

In this section we present the algorithm used to obtain a distortion calibration map. The algorithm considers imaging a star field at two different epochs to measure a change in the position of the host star with respect to the background, creating two images with spikes called I_1 and I_2. Also, a reference image I_{ref} is obtained as the sum of I_1 and I_2 and a different image I_{diff} is computed as a subtraction of them. The next step in the data reduction process is to calculate Cartesian unitary derivatives of the difference image, which are obtained by taking I_{diff} and subtracting it by a 1 pixel shifted version of itself, first in x and afterwards in y, resulting in two derivative frames in Cartesian coordinates. Then the Cartesian derivative terms are used to compute the angular derivative:

$$\frac{\partial I_{diff}}{\partial \theta} = -y\frac{\partial I_{diff}}{\partial x} + x\frac{\partial I_{diff}}{\partial y} \tag{2}$$

Having obtained the angular derivative for every pixel on the image, the next step is to calculate the angular distortion performing a pixel-to-pixel division of the different image with the angular derivative:

$$\theta_{disp} = \frac{I_{diff}}{\frac{\partial I_{diff}}{\partial \theta}} \tag{3}$$

At this step, the noise problem arises since the distortions to be measured are in the range of 10^{-2} to 10^{-5} pixel. Therefore, the value of the pixels with signal along the spikes will be in this range. However, in all other locations of the image where there are no spikes present in the image the noise level is orders of magnitude higher that the signal value on the spikes. To solve this problem, a distortion Signal to Noise Ratio (SNR) ratio matrix for every pixel on the image is computed. In this expression the signal is the value of the angular derivative and the noise is computed as the root sum square of the readout noise plus the photon noise,

$$SNR = \frac{\frac{\partial I_{diff}}{\partial \theta}}{Noise}. \tag{4}$$

The square of the SNR matrix is applied to the angular distortion matrix amplifying the values along the spikes and minimizing it on the background,

$$\theta_{disp\_SNR} = \theta_{disp} SNR^2. \tag{5}$$

To reduce the noise level along the spikes, the image is binned. Then the angular distortion matrix is divided by the binned version of SNR^2 to recover the correct values on the angular distortion matrix. In this matrix, the pixel value represents the angular distortion for its location in units of pixel size, i.e. a value of 1 represents 7.4μm of angular distortion at that location on the chip. However, distortion values are only available along the spikes. Then, an interpolation process is needed to assign distortion values for the pixels between the spikes. Here, the original design of the diffractive pupil plays a fundamental role since its periodicity and geometry defines the angular separation of the spikes determining the interpolation process. Since dynamic distortions are caused by local flexures of the optical surfaces on the system, only relatively low spatial frequency distortion changes are expected, and therefor the frequency of the spikes has to be chosen to properly sample the distortion changes.

After the SNR^2 angular distortion or θ_{dist_SNR} matrix is obtained, it is recommended to bin the data to make the interpolation process less computationally intensive. At this point the SNR^2 and the θ_{dist_SNR} are binned by factor of ten to obtain the SNR^2_{bin} and $\theta_{dist\_SNR\_bin}$ matrices of 250x250. Those matrices can be interpolated by performing the convolution with an interpolation function g,

$$\theta_{dist\_SNR\_bin\_interp} = \left(\theta_{dist\_SNR\_bin}\right) * g\ , \tag{6}$$

where g is a normalized Gaussian kernel defined as,

$$g = Ae^{-\left(\frac{x^2+y^2}{2\sigma^2}\right)}, \tag{7}$$

where A=1 to have a normalized value and σ defines the FWHM of the Gaussian kernel. Controlling σ or the FWHM of the Gaussian kernel will define how aggressive the interpolation is and therefore sets the maximum spatial frequency contained in the distortion map. This is set as a parameter in the algorithm that can be adjusted to match the highest spatial frequency distortion expected in the system.

Here, the original design of the diffractive pupil and the correct selection of the kernel size play fundamental roles since the periodicity and geometry define the angular separation of the spikes determining the interpolation process. Since dynamic distortions are caused by local flexures of the optical surfaces in the system, only relatively low spatial frequency distortion changes are expected, and therefore the frequency of the spikes has to be chosen to properly sample the distortion changes. Finally to recover the real values of the angular distortion it is necessary to divide the $\theta_{dist\_SNR\_bin}$ by the $SNR^2_{bin\_interp}$ matrix,

$$\theta_{dist\_real} = \frac{bin(\theta_{dist}SNR^2)*g}{bin(SNR^2)*g} \tag{8}$$

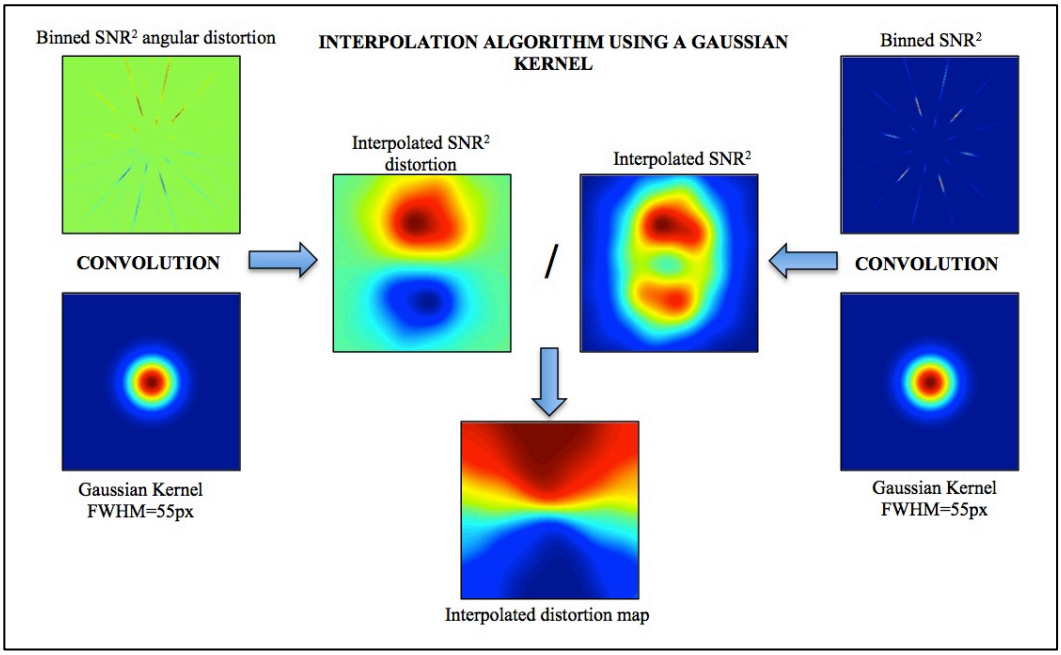

Figure 7. The image on the left shows the substrate with the concentrator lens glued in the back. The image on the right shows the simulated star field

A flow diagram of the interpolation process using real data is shown in Figure 7. Note that the images displayed correspond to the 0.5px right shift test performed. The 55px FWHM Gaussian kernel is shown to scale. The result is θ_{dist_real}, which is a binned distortion map with valid values for every pixel in the field.

4.2 Astrometric Tests

To compute the astrometric correction to be applied to the image based on the distortion map, a couple of artificial distortion modes were generated for half pixel translations of the image in X and Y-axis, called D_x and D_y. Then, the measured distortion map was decomposed in a linear combination, with coefficients a_1 and a_2 of the unitary distortion basis,

$$D_{measured} = a_1 D_x + a_2 D_y \ . \tag{9}$$

Since the basis is not orthogonal, an iterative solver, which uses the dot product of the basis with the distortion map, was implemented. The estimated values of the coefficients $\hat{a}_1 \ and \ \hat{a}_2$ were summed over all the iterations to find the estimated coefficient values that corresponded to the astrometric correction Ac_x and Ac_y to be applied to the centroiding measurements to obtain the corrected astrometric signal Ac_x and Ac_y.

$$A_x = \left[\frac{\sum_{i=1}^{N_S}(P_{1x}(i) - P_{2x}(i))}{N_{star}} - Ac_x\right], \ A_y = \left[\frac{\sum_{i=1}^{N_S}(P_{1y}(i) - P_{2y}(i))}{N_{star}} - Ac_y\right] \tag{10}$$

To test this approach, the astrometric signal of the central star has been measured with respect to the background stars. Since there is no real astrometric signal, any measured value is caused by distortions in the optical system or detector movements and imperfections. For this test, two 360s exposures where taken with a delay of 12 minutes. During the total integration time including the delay, a thermal shift of approximately 0.5˚ C was measured in the laboratory. Any thermal change moves the star simulator and the camera up by thermal expansion of the supports, but since the optical system has a magnification of -1, the image goes down causing thermal sensibility of 7.4µm/ ˚C or 1px/ ˚C along the vertical axis. Additionally, we observe a crosstalk on the horizontal axis caused by the mount of the off-axis parabolas, which in reality are full parabolas supported from the mechanical axis. Therefore, the off-axis illuminated portion causes slight shifts on the horizontal axis due to thermal effects. Here we compare the astrometric signal measured using three different approaches.

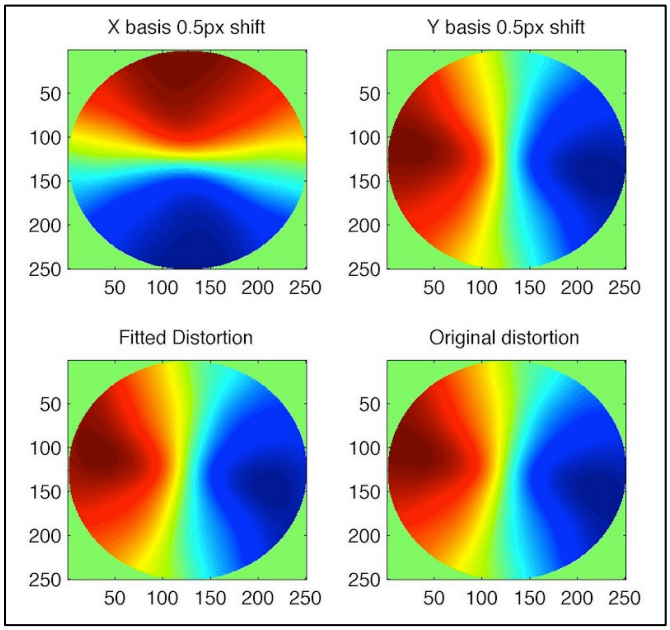

Figure 8. The top row shows the distortion calibration basis. The bottom row shows the fitted distortion and on the left and the measured one on the right.

In this experiment the light of the central star has been blocked by the coronograph. For the first approach, where the CCD is used as a reference, only the array of background stars can be seen and the detector coordinates are used as a reference for the astrometric measurement. After removing saturated and noisy stars, the total number of stars is reduced to 207. Then, the centroid for each star is calculated using the Center of Gravity algorithm along the X axis and Y-axis for the first epoch. The same procedure is repeated for the second epoch or image to obtain the second sets of stars. Then, the astrometric signal A_x and A_y is computed as the average difference of the two epochs stars' coordinates. The

results obtained provide an astrometric signal of A_x = 0.0357px and A_y =-0.4753px, which is equivalent to a modulus of the astrometry error vector of 0.4767px. Most of this error is attributable to thermal shifts because the error vector is mostly aligned along the Y-axis where those errors can manifest.

Now we consider a second case where we will assume that the central host star is not blocked or somehow its position is recovered from the coronagraph. For this purpose another star was selected close to the center field, which can simulate the role of the central star to calibrate the pointing and low order effects on the image plane. This is a bright but not saturated star, and its centroid was computed and subtracted to the average value of the rest of the stars. Since there is no astrometric signal generated at the central star, the differential measurement between the host star and the background stars should be zero. Using the correction of the host star the new astrometry measurement reports A_x=0.0269px and A_y = 0.0104px, which is equivalent to a modulus of the astrometry error vector of 0.0288px. The astrometric error vector using the host star is only 6% of the initial case without the host star. This represents a significant improvement of this technique.

When the distortion map, shown in Figure 8, and the basis fitting algorithm are used to calibrate the astrometric signal, the measurement reports A_x = -0.00032px and A_y = -0.0123px, which is equivalent to a modulus of the astrometry error vector of 0.0123px. This astrometric error vector calibrated with the diffractive distortion map is only 2.58% of the astrometric error measured with the initial case, where the CCD is used as reference and a reduction to 42% of the error measured using the position information of the host star.

This result shows that astrometric precision can be improved by a factor of more than two using this technique with respect to a traditional centroiding method using host star centroid calibration. Additionally, an important advantage of this technique is the capability of achieving this performance without the need of a host star, enabling the coronographic/ direct imaging mode at the same time. A summary of the results for each the three techniques previously described are presented in Table 2.

Table 2. Summary of the astrometric measurements results

	Background stars average [px]		Correction [px]		Residual astrometric signal [px]		Residual vector [px]	Percentage of original error
Technique	$\bar{P}_{1x}$	$\bar{P}_{1x}$	Ac_x	Ac_x	A_x	A_x	$\lvert\vec{A}\rvert$	%
CCD	0.0357	-0.4753	NA	NA	0.0340	-0.4604	0.4617	100.0%
Host-star	0.0357	-0.4753	0.0089	-0.4858	0.0269	0.0104	0.0288	6.04%
Diffractive pupil	0.0357	-0.4753	0.0354	-0.4877	0.00034	-0.0123	0.0123	2.6%

If an aperture scaling criteria were applied to simulate a 1.4m telescope, the residual astrometric error would be 390 microarcseconds. This error is 22 times larger than the scaled theoretical performance of 18 microarcseconds that this technique could achieve in this laboratory. However, the conditions of this test are not optimal in the following aspects: the centroding precision can be improved with a lower read out noise and applying PSF fitting and matched filters techniques and the distortion calibration has to be applied also to high order distortion modes and not only tip-tilt. Even without any improvement this experiment has validated the concept proving that it can improve the astrometric measurements.

4.3 Compatibility with Coronography

The goal of this experiment is to demonstrate that the Diffractive Pupil concept is compatible with high contrast imaging techniques in the same telescope. This requires the diffractive orders on the image plane to be located outside the FoV of the coronagraph, which by design should be attainable. However, manufacturing problems, such us low frequency variations on the spacing of the diffractive pupil dots, could generate unexpected diffraction orders inside the FoV. For this experiment we used the high contrast test bed[6] at NASA Ames. This test bed was designed to work down to 10^{-9} contrast levels using a PIAA coronograph, a Deformable Mirror (DM) to correct the wavefront, and a Focal Plane Occulter to mask the source. The bench was in air and thermally stabilized to +/- 0.002 K. The system has demonstrated contrast levels of $2x10^{-8}$ raw contrast in an annular region that spans from 2.0 to 3.4 λ/D.

The diffractive pupil has to be installed on or close to a pupil plane. Given the optical layout of the bench, the only available pupil plane was downstream from the PIAA coronograph where the DM was located. The DM was removed and a translation stage was installed. On the stage a flat mirror, with surface quality of λ/10 at 633nm, and the diffractive pupil dotted mirror were installed and aligned. To select the diffractive pupil or the flat mirror, the stage was translated.

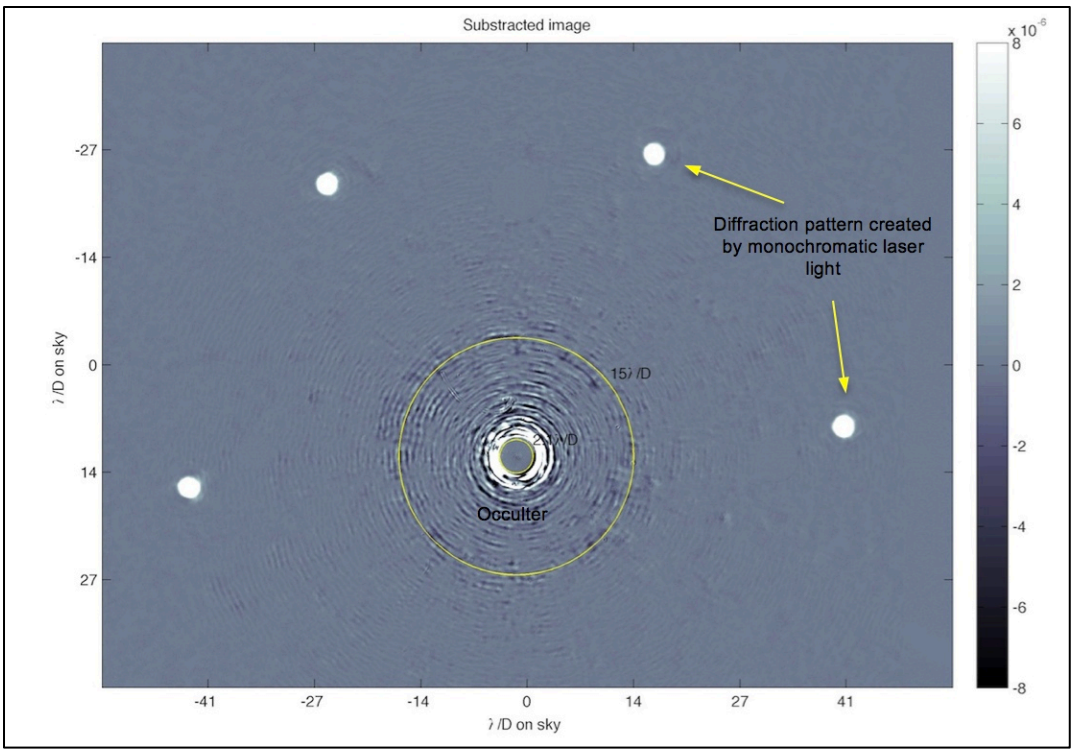

Figure 9. Differential image of a flat and diffractive mirror images. Monchromatic diffractive orders are shown at 44λ/D. No evidence diffractive contamination is detected, however our detectability limit varies with field angle due to occulter ringing.

After analyzing a differential image created using a flat mirror and the diffractive pupil mirror, shown in figure 9, we find that there is no diffractive contamination down to a contrast level of $2x10^{-7}$ over the region outside 16λ/D. If the morphology of the features are excluded from the contrast envelope, this result can be extended inside the region spanning from 5 to 16λ/D. Inside the region spanning from 12 to 16λ/D, the contrast is limited to $2x10^{-6}$ ring patterns, which are probably created by the occulter, and coherently amplified. Also, we note that between 8 and 12λ/D the contrast envelope gets tighter, down to a contrast level of $5x10^{-7}$ and finally increasing to $2x10^{-6}$ inside the region of 5 to 8λ/D.

The region spanning from 2 and 5λ/D is dominated by ringing features. As their intensity is maximally close to the occulter, a small misregistration of the images or shape change creates large contrast artifacts on the subtracted image. We ran the image registration optimization routine again setting the region of interest from 2 to 5λ/D. After performing this optimization, we found no diffractive contamination up to a contrast envelope of $5x10^{-6}$ within this region. Moreover, we consider it highly unlikely that diffractive features can appear in the region spanning from 2 to 5λ/D if no features have been detected at larger angles because it would require a single and very low spatial frequency component on the array of dots imprinted on the diffractive mirror.

A summary of the contrast regions and their contrast limits to detect diffractive contamination is presented in Table 3. The limiting factors are ring-like features probably caused by coherent amplification of the different wavefront error sources of the optics. Within this limit, we did not find evidence of diffractive contamination with morphological features that can be generated by a hexagonal dot pattern imprinted on the mirror. This argument suggests that there is no contamination of the IWA to deeper contrast levels; however, this cannot be demonstrated until we can enable the

wavefront control to suppress the ringing effect. We plan to repeat the experiment when this configuration becomes available.

Table 3. Detection limit versus angular separation, no contamination was found within this range.

Detection limit criteria	Angular separation				
	2 - 5λ/D	5 - 8λ/D	8 - 12λ/D	12 - 16λ/D	> 16λ/D
Contrast envelope cut	$5.0x10^{-6}$	$2.0x10^{-6}$	$5.0x10^{-7}$	$2.0x10^{-6}$	$2.0x10^{-7}$

5. FUTURE WORK AND CONCLUSIONS

A high precision astrometry laboratory has been designed an implemented to simulate and test the operation of the diffractive pupil distortion calibration. The test bed is functional now, and the ability of the dotted pupil to generate the diffractive spikes with polychromatic light has been demonstrated proving that the concept is able to improve the accuracy of the astrometric measurements by calibrating the field distortions.

Also it was proven that this concept enables simultaneous high contrast imaging and high-precision astrometry on a single mission because the astrometric measurement does not use the light of the central star for the astrometric measurements. Therefore, light can be redirected to a coronagraph to perform high contrast imaging.

Also, we demonstrated the manufacturability of small-scale diffractive mirrors using lithography, and it has been demonstrated in the laboratory that real diffractive pupils are precise and regular, avoiding diffractive contamination of the IWA of the image due to low spatial frequency modulation of the spots' spacing or any other effects.

Future plans are to implement this system at the NASA Ames high contrast imaging test bed to enable for the first time a laboratory that would test the high contrast imaging capabilities with the wide field high precision astrometry, serving as a demonstration for a future exoplanet detection flagship mission.

ACKNOWLEGMENTS

This project is funded by NASA grant 09-APRA09-0140 program and has received help and advice of the following people in different aspects of the project: Michael Shao, Stuart Shaklan, Robert Woodruff, Jim Burge, Roger Angel, Marie Levine, Josh Eisner. Finally, this project acknowledges the support of the Institute of International Education IIE with their Fulbright PhD Science and Technology program.

REFERENCES

[1] Holtz, Robert, "Scientists Uncover Evidence of New Planets Orbiting Star," *The Tech* (1992).

[2] Shao, M., Catanzarite, J. and Pan, X., "The synergy of direct imaging and astrometry for orbit determination of exo-earths," Astrophysical Journal 720(1), 357-367 (2010).

[3] Guyon, O., Bendek, E., Eisner, J., Angel, R., Woolf, N., Milster, T., Ammons, M., Shao, M., Shacklan, S., Levine, M., Nemati, B., Pitman, J., Woodruff, R., and Belikov, R., "High precision astrometry with a diffractive telescope," Astrophysical Journal 200:11, 22 (2010).

[4] Guyon, O., Shaklan, S. B., Levine, M. B., Cahoy, K. L., Tenerelli, D. J., Belikov, R., Kern, B. D., "The pupil mapping exoplanet coronagraphic observer (PECO)," Proc. SPIE 7731, 7731-80 (2010).

[5] Smith, W., "Modern Optical Engineering," SPIE Press McGraw-Hill, Bellingham (2000).

[6] Belikov, R., Pluzhnik, E., Connelley, M., Witteborn, F., Greene, T., Dana, L., Zell, P., Guyon, O., "Laboratory demonstration of high-contrast imaging at 2 λ/D on a temperature-stabilized testbed in air," Proc. SPIE 7731, 77312D-2D11 (2010).